Iterative Learning Control of Functional Electrical Stimulation Electrode Arrays

Lucy Hodgins, Chris T. Freeman and Zehor Belkhatir

***Abstract*—Stroke often causes weakness, paralysis, or loss of coordination in the hand and wrist, making it difficult to perform everyday tasks. Current rehabilitation approaches do not adequately assist patients in regaining their lost function, however it is possible to produce accurate hand and wrist gestures by artificially stimulating muscles using functional electrical stimulation (FES) applied to multi-element electrode arrays. This has been possible using iterative learning control (ILC), however it required lengthy model identification tests, and accuracy degraded due to fatigue, spasticity and changes in array position.**

This paper develops a new FES electrode array control framework which maintains high accuracy despite uncertain and potentially time-varying dynamics. First a model of stimulated hand and wrist dynamics embedding FES array misalignment is developed, and robust stability properties are derived using the gap metric. A compensating controller is then proposed to ameliorate array misalignment, and this is integrated within a powerful framework termed estimation-based multiple-model ILC (EMMILC), which automatically updates the underlying model to maintain performance in the presence of uncertain and changing dynamics. It is shown that EMMILC can remove the need for model identification, whilst maintaining high performance. This significantly improves the usability of FES arrays and opens up the possibility of bringing effective therapy to millions of patients in their own homes. Experimental results reveal that the proposed controller reduces the average converged error norm to 31.3% of that obtained using existing model-based ILC.

***Index Terms*—Iterative Learning Control, Functional Electrical Stimulation, Multiple Model Switched Adaptive Control, Stroke Rehabilitation, Electrode Arrays**

I. INTRODUCTION

STROKE is a leading cause of disability worldwide, with over 12 million new cases each year [1]. Up to 80% of stroke survivors suffer from upper limb impairment [2], and only 11% of patients fully recover dexterity [3], impacting their lives in numerous ways; over 50% cannot manage personal hygiene (bathing, toilet use, grooming) independently, and 40% need help with dressing and feeding [4]. Movement can be regained through continued repetitive practice of functional tasks, which strengthens neural connections in the brain (Hebbian learning [5]). Patients typically receive half an hour of conventional therapy, three times per week [6], which involves a physiotherapist manually assisting their movement. This is far less that the three hours of daily therapy recommended by clinical guidelines [7], and results in 62% of people with severe impairment failing to regain dexterous hand motion within six months [3].

Assistive technologies can potentially solve this problem by providing high doses of therapy at low cost. The most common is functional electrical stimulation (FES) [8], which stimulates nerves using surface electrodes to artificially contract the underlying muscles. FES for upper limb rehabilitation after stroke has been shown to be clinically-effective [9], [10], and cost-efficient [11]. There are many commercial FES systems such as MyndMove (MyndTec Inc, ON, Canada), but they all require the user to position several large electrodes each time they don the system, often taking 10 minutes. They are typically open-loop and can only achieve crude movements.

Researchers have begun to address the limitations of commercial devices by developing transcutaneous electrode arrays comprising multiple electrode pads integrated in a single structure [12]–[15] (an example is shown in Fig. 1a)). These are able to selectively stimulate the numerous muscles needed for hand movement [16]. Most controllers mimic the way a physiotherapist manually positions electrodes by automatically cycling through different pad locations until a satisfactory response is achieved (measured using angle sensors). This set-up procedure takes 10-15 minutes each time it is used, and stimulation is then applied at the optimum location using open-loop or triggered control [17]–[19].

More sophisticated FES array controllers have improved tracking accuracy of functional movements. A recurrent fuzzy neural network was able to accurately produce a range of hand movements but required 45 minutes to set-up and train each time it was used [20]. It also required impulsive inputs that would be uncomfortable for patients. The highest accuracy was achieved using iterative learning control (ILC), which updated the FES array signals using data from repeated attempts at the task [21], [22]. ILC's ability to learn over successive 'trials' of a tracking task matches the repetitive nature of rehabilitation, and it has previously proved successful in five clinical trials with stroke participants [23]. When ILC was applied to FES arrays, it assisted simple hand movements (pointing, pinching, opening) which were chosen based on clinical need since patients typically cannot extend their wrist and fingers. The ILC update required a model, and so identification tests were performed between each trial. This involved stimulating all 24 electrode array elements individually and fitting a local linear model to the resulting joint angular movements. After three trials of ILC the mean joint angle error was reduced to below 5° for the 10 participants tested [15]. Unfortunately the process took over 10 minutes for each gesture.

The problem facing all these controllers is that the muscle dynamics change rapidly, and are very sensitive to array

---

This work was supported by the U.K. Engineering and Physical Sciences Research Council.

L. Hodgins, C. Freeman and Z. Belkhatir are with the School of Electronics and Computer Science, University of Southampton, Southampton, UK, SO16 7BT. (email: lgh1g19@soton.ac.uk; ctf1@soton.ac.uk; Z.Belkhatir@soton.ac.uk)

position that inevitably changes from day to day. The system dynamics and the task are both complex: [24] reports there are 17 grasp types used in daily activities, illustrating the gap between current systems and a practical clinical solution.

This paper makes several contributions to solve the problem of FES array control, including:

- The first comprehensive model of an FES array applied to an artificially activated musculoskeletal system is developed.
- Robust performance bounds are derived for a general class of ILC updates applied to the system. These extend previous robustness results by allowing the ILC update to vary between trials (thereby matching the ILC updates used for FES arrays [15]).
- The effect of array misalignment is modelled and its detrimental effect on system robust performance is quantified.
- A control scheme is developed to correct for misalignment, which maximises robust performance. This is the first controller to tackle array misalignment aside from [21], which dealt with only the simple case of translation by an integer number of pads.
- The resulting ILC update is then embedded in a multiple model switched adaptive framework. This new architecture allows ILC to automatically switch between a set of models that are designed in advance to capture all possible uncertainty. This enables it to maintain high accuracy despite changing muscle dynamics and array positions. This 'estimation-based multiple model ILC' (EMMILC) framework extends the authors' previous implementation [25], [26] to include nonlinear dynamics, and provides guaranteed performance over an uncertainty space that is defined by the designer. The analysis uses the gap metric, a well-known measure of difference between plants that does not impose structural assumptions on dynamics. This is the first multiple model ILC framework to provide guaranteed performance bounds for an unstructured uncertainty space specified by the designer.
- Numerical results applying EMMILC to a realistic FES array model are presented for hand and wrist motion control. These confirm higher accuracy than all existing controllers, while requiring no model identification (after a single initial set-up session). Experimental results similarly confirm higher accuracy than existing controllers.

These contributions not only solve the FES array problem, but can also be applied to a wide variety of systems including EMG arrays and implantable intracortical microelectrodes. They enable high tracking accuracy to be achieved whilst removing the need for model identification and controller tuning that prevents widespread transference to clinical practice or home use. The EMMILC architecture therefore has utility to improve any practical application of ILC.

This paper is structured as follows. Section II defines the control problem and introduces a comprehensive model of the hand and wrist stimulated by an FES array. Robust performance bounds are derived in Section III. Section IV shows the performance degradation caused by misalignment, and develops an optimal compensation controller. Section V presents the non-linear EMMILC framework, which delivers guaranteed tracking performance for any system dynamics belonging to a specified plant uncertainty set. A detailed design framework is provided to realise practical efficacy and is evaluated numerically and experimentally in Sections VI and VII respectively, before Section VIII concludes the paper.

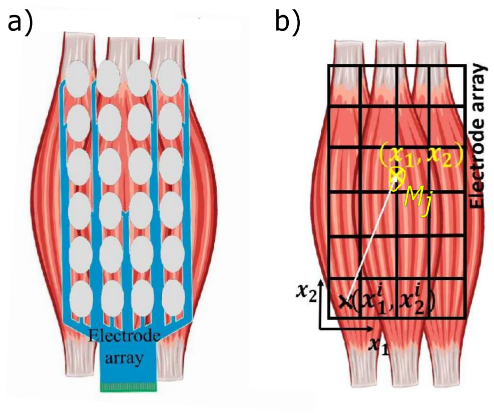

Fig. 1. (a) Surface array overlaying muscles, (b) coordinates of pad i and muscle j with neuromuscular junction M_j.

II. PROBLEM DESCRIPTION

The aim of rehabilitation is to assist the patient to complete a functional movement over multiple attempts. The movement is defined by selecting q clinically-relevant joint angles $y \in \mathcal{L}_2^q[0,T]$ and defining a corresponding reference trajectory $y_d \in \mathcal{L}_2^q[0,T]$ that the patient must track over a finite test duration T. One or more FES electrode arrays are positioned over the muscles that must be assisted to help the patient complete the movement.

FES electrode arrays are composed of n separate electrode pads, that are arranged in fixed pattern. Pads are usually arranged in a grid rather than being aligned with muscle locations, giving the clinician freedom to adjust which electrodes are active based on the patient's response. This also removes the need to manufacture personalised array geometries for each patient, and then place them exactly over the intended muscles. Arrays are typically printed on polycarbonate and have a hydrogel layer that is placed on the surface of the skin, although fabric arrays are also emerging. Over the test duration a sequence of electrical pulses, $u \in \mathcal{L}_2^n[0,T]$, is applied to these electrodes in order to generate an electric field to artificially enervate the underlying muscles. This causes them to contract and actuate joints that are connected to the muscles via tendons. A full model is derived next.

A. Hand and Wrist Model Structure

The dynamics of the electrically stimulated hand and wrist consist of four key components: the electrode array, the muscle dynamics, the non-linear tendon network, and the biomechanical rigid body dynamics [27]. A model of an FES array has been proposed in previous literature, but without formal justification. This is provided next:

Definition 1: Consider an n pad FES array, where the ith pad has a centre position $x^i = (x_1^i, x_2^i)$ and receives the stimulation sequence, $u_i(t)$ at time t. Let the array be placed over l underlying muscles, each with a neuromuscular junction with surface $\mathcal{M}_j$ defined in the same coordinate system, as shown in Fig. 1b). Then the enervation, $v_j(t)$, $j = 1, \dots, l$, delivered to these muscles is given by

$$v(t) = Au(t), \tag{1}$$

where the fixed matrix $A \in \mathbb{R}^{l\times n} \geq 0$ has elements

$$A_{j,i} = \oiint_{\mathcal{M}_j} \underbrace{\frac{\kappa}{\|x - x^i\|^2}}_{E_i(x)} dx_1 dx_2, \quad \begin{array}{l} j = 1, \dots, l \\ i = 1, \dots, n \end{array} \tag{2}$$

in which $E_i(x)$ denotes the electric field at point $x = (x_1, x_2)$ due to the ith electrode pad, and κ is a constant.
Proof. See Appendix A. $\square$

The force generated by the jth muscle in response to enervation $v_j(t)$ can be accurately captured by a Hammerstein structure, comprising a static function $h_{IRC,j}(v_j(t))$ which models the isometric recruitment curve (IRC), cascaded with linear activation dynamics (LAD), denoted $H_{LAD,j}$ [28]. A bounded multiplicative term $\hat{F}_{m,j}(y(t), \dot{y}(t))$ is also required to model the effect of joint angle and joint angular velocity on the active force $f_j(t)$ [29]. The resulting force $\hat{f}_j(t)$ then feeds into a tendon network which develops a moment about each joint angle given by

$$\tau(t) = R(y(t))\hat{f}(t), \tag{3}$$

where element (i, j) of moment arm matrix $R(y(t))$ is equal to $\frac{dE_j(y_i)}{dy_j}$, in which continuous function E is the associated tendon excursion defined in [30]. Moment vector $\tau(t)$ then actuates the passive rigid body dynamics of the system which take the standard form

$$M(y(t))\ddot{y}(t) + C(y(t), \dot{y}(t)) + K(y(t), \dot{y}(t)) = \tau(t) \tag{4}$$

where $M(\cdot)$ denotes the inertia matrix, $C(\cdot,\cdot)$ is the Coriolis matrix, and $K(\cdot,\cdot)$ captures gravity, joint stiffness, damping and friction effects.

The overall along-the trial system mapping is hence

$$\begin{aligned} G^* &: \mathcal{L}_2^n[0,T] \to \mathcal{L}_2^q[0,T] \\ &: u \mapsto y : y = H_{RB} F_m H_{LAD} h_{IRC} A u \end{aligned} \tag{5}$$

with elements defined by the operators

$$\begin{aligned} A &: \mathcal{L}_2^n[0,T] \to \mathcal{L}_2^l[0,T] : u \mapsto v : v = Au \\ h_{IRC} &: \mathcal{L}_2^l[0,T] \to \mathcal{L}_2^l[0,T] : v \mapsto w : w_j = h_{IRC,j} v_j \\ H_{LAD} &: \mathcal{L}_2^l[0,T] \to \mathcal{L}_2^l[0,T] : w \mapsto f : f_j = H_{LAD,j} w_j \\ F_m &: \mathcal{L}_2^l[0,T] \to \mathcal{L}_2^q[0,T] : f \mapsto \tau : \tau_i = \sum_j F_{m,i,j} f_j \end{aligned}$$

where $F_{m,i,j} = R_{i,j}(y)\hat{F}_{m,j}(y, \dot{y})$, $j = 1, \dots, l$, and

$$\begin{aligned} H_{RB} &: \mathcal{L}_2^q[0,T] \to \mathcal{L}_2^q[0,T] : \tau \mapsto y \\ &: \ddot{y} = M(y)^{-1}(\tau - C(y, \dot{y}) - K(y, \dot{y})) \end{aligned} \tag{6}$$

This system is summarised in Fig. 2.

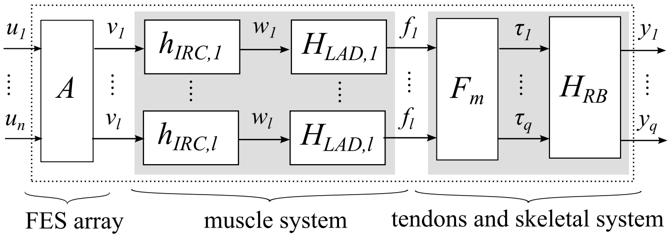

Fig. 2. Hand and wrist system G^* showing underlying structure.

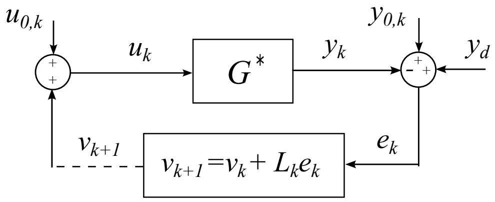

Fig. 3. ILC feedforward configuration, applied to true plant G^*. The dashed line denotes trial-to-trial memory.

B. Tracking Objective

The rehabilitation control objective is for the joint angles y, generated by system (5), to track the reference signal $y_d \in \mathcal{L}_2^q[0,T]$. ILC does this by performing repeated attempts, termed 'trials', in which the FES input u is updated using data from the previous trial. The subscript $k = 1, 2, \dots$ is therefore introduced on each signal to denote the trial number, producing the system shown in Fig. 3. Here $u_{0,k}(t)$, $y_{0,k}(t)$ are external disturbances acting on the system input, u_k, and output, y_k.

The most common form of ILC update has form

$$v_{k+1} = v_k + L_k e_k, \tag{7}$$

in which $e_k = y_d + y_{0,k} - y_k$ is the tracking error and $L_k : \mathcal{L}_2^q[0,T] \to \mathcal{L}_2^n[0,T]$ is a suitably chosen learning operator (see, e.g. [31]). Since the true dynamics are unknown, design of L_k is based on an assumed model G. A common choice is to design L_k to satisfy the operator norm bound

$$\|I - L_k G_k\| < 1, \quad \forall k \in \mathbb{N}_+ \tag{8}$$

where G_k is the linear approximation of the system dynamics about operating point u_k, i.e. $G|_{u_k} u := G(u+u_k) - Gu_k$. If (8) holds, it is well-known that the system will then monotonically converge to the minimum error, e.g.

$$\lim_{k\to\infty} e_k(t) = 0, \quad t \in [0,T]. \tag{9}$$

provided the true system is linear, $n = q$, and there is no model error or disturbance. There are also robustness results that specify the allowable model uncertainty for convergence to minimum error, but only for special forms of L_k, i.e. P-type, gradient and Newton ILC [32] or for a fixed L_k [33]. For general L_k, and arbitrary true system G^* dynamics, there is no guarantee that applying ILC law (7) will result in convergence.

The next section addresses this by establishing conditions for convergence using a general measure of plant mismatch. This shows how L_k can be selected to maximise robust performance.

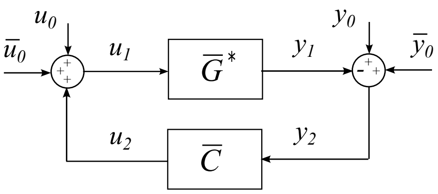

Fig. 4. ILC feedback configuration represented in lifted domain, with plant input and output ($i = 1$), disturbances ($i = 0$) and observations ($i = 2$).

III. ROBUST PERFORMANCE

The nonlinear gap δ is an established measure of the distance between two systems, which is extensively used in the field of robust control [34]. It enables stability analysis to be carried out without placing restrictive assumptions on the structure of the uncertainty [35]. To apply gap based robust stability results to ILC, it is first necessary to reformulate the finite-duration, $t \in [0, T]$, along-the-trial feedforward dynamics of Fig. 3 to take the conventional feedback form shown in Fig. 4. This is done by introducing lifted signal spaces

$$y_i \in \mathcal{Y}, \quad u_i \in \mathcal{U}, \quad w_i = (u_i, y_i)^\top \in \mathcal{U} \times \mathcal{Y} \tag{10}$$

for the disturbances, plant and controller, $i = 0, 1, 2$ respectively, and

$$\bar{y}_0 \in \mathcal{Y}, \quad \bar{u}_0 \in \mathcal{U}, \quad \bar{w}_0 = (\bar{u}_0, \bar{y}_0)^\top \in \mathcal{U} \times \mathcal{Y} \tag{11}$$

for the external biases. Using the lifted spaces $\mathcal{U} = \mathcal{L}_2^n[0, T] \times \mathbb{N}$, $\mathcal{Y} = \mathcal{L}_2^q[0, T] \times \mathbb{N}$, the signals appearing in Fig. 3 can be packaged as

$$\begin{aligned} &u_k = u_1(k),\ v_k = u_2(k),\ u_{0,k} = u_0(k),\ 0 = \bar{u}_0, \\ &y_k = y_1(k),\ e_k = y_2(k),\ y_{0,k} = y_0(k),\ y_d = \bar{y}_0, \end{aligned} \tag{12}$$

for $k \in \mathbb{N}_+$. The plant and ILC dynamics over $t \in [0, T]$ of the k^{th} trial are then expressed equivalently as a single time instant of the 'lifted' systems

$$\bar{G}^* : \mathcal{U} \to \mathcal{Y} : u_1 \mapsto y_1 : y_1(k) = G^* u_1(k) \tag{13}$$

and

$$\bar{C} : \mathcal{Y} \to \mathcal{U} : y_2 \mapsto u_2 : u_2(k+1) = u_2(k) + L_k y_2(k). \tag{14}$$

Having reformulated ILC in standard feedback form, gap-based robustness analysis can now be applied [35]. The dynamics of closed-loop system $[\bar{G}^*, \bar{C}]$ are governed by the parallel projection operator

$$\Pi_{\bar{G}^*//\bar{C}} : \mathcal{U} \times \mathcal{Y} \to \mathcal{U} \times \mathcal{Y} : (w_0 + \bar{w}_0)^\top \mapsto w_1 \tag{15}$$

mapping external disturbances to the internal plant signals. Closed-loop stability is defined using the biased norm $\|w_1\|_{\bar{w}_1} = \|w_1 - \bar{w}_1\|$ which measures the distance of internal plant signals w_1 from their nominal operating point $\bar{w}_1 := \Pi_{\bar{G}^*//\bar{C}} \bar{w}_0$. This leads to the definition:

Definition 2: ILC system $[\bar{G}^*, \bar{C}]$ is said to be gain stable with respect to the external bias $\bar{w}_0 = (0, y_d)^\top$ if there exists a scalar $0 < M < \infty$ such that

$$\|\Pi_{\bar{G}^*//\bar{C}}\|_{\bar{w}_0} = \sup_{w \in \mathcal{U} \times \mathcal{Y}} \frac{\|\Pi_{\bar{G}^*//\bar{C}} w - \Pi_{\bar{G}^*//\bar{C}} \bar{w}_0\|}{\|w - \bar{w}_0\|} < M. \tag{16}$$

To examine ILC robust performance, let the system used to design the ILC update be defined as

$$\bar{G} : \mathcal{U} \to \mathcal{Y} : u_1 \mapsto y_1 : y_1(k) = G_k u_1(k), \tag{17}$$

then the following theorem gives conditions under which the ILC update designed using model (17) is able to stabilise the true plant $\bar{G}^*$ defined in (13).

Theorem 3: Let ILC update $\bar{C}$ (14) be designed using model $\bar{G}$ such that condition (8) holds. Then the true closed-loop system $[\bar{G}^*, \bar{C}]$ is BIBO stable if the gap[1] satisfies

$$\delta(\bar{G}^*, \bar{G}) < \|\Pi_{\bar{G}//\bar{C}}\|_{\bar{w}_0}^{-1}. \tag{18}$$

where the parallel projection operator norm $\|\Pi_{\bar{G}//\bar{C}}\|_{\bar{w}_0}$

$$\leq \sup_{k \in \mathbb{N}_+} \left\| \begin{pmatrix} I \\ G_k \end{pmatrix} \right\| \left(1 + \frac{\sup_{k \in \mathbb{N}_+} (\|L_k\| + \|L_k G_k\|)}{1 - \sup_{k \in \mathbb{N}_+} \|I - L_k G_k\|} \right). \tag{19}$$

The converged signals are then bounded as

$$\|\Pi_{\bar{G}^*//\bar{C}}\|_{\bar{w}_0} \leq \|\Pi_{\bar{G}//\bar{C}}\|_{\bar{w}_0} \frac{1 + \delta(\bar{G}^*, \bar{G})}{1 - \|\Pi_{\bar{G}//\bar{C}}\|_{\bar{w}_0} \delta(\bar{G}^*, \bar{G})}. \tag{20}$$

Proof See Appendix B. □

The gap $\delta(\bar{G}^*, \bar{G})$ in (18) can be related to how well the model G_k captures the true dynamics G^* at each operating point using the next theorem.

Theorem 4: The nonlinear gap $\delta(\bar{G}^*, \bar{G})$ between the true plant $\bar{G}^*$ and the sequence of linear models $\bar{G}$ can be directly related to individual linearisations using

$$\delta(\bar{G}^*, \bar{G}) \leq \sup_{k \in \mathbb{N}_+} \delta(G^*, G_k) \leq \sup_{\substack{\|u\| \neq 0, \\ k \in \mathbb{N}_+}} \frac{\|(G^*|_{u_k} - G_k) u\|}{\|u\|}. \tag{21}$$

Proof Given in [33]. □

Hence $\delta(\bar{G}^*, \bar{G})$ can be replaced throughout Theorem 3 by either the along-the-trial form $\sup_{k \in \mathbb{N}_+} \delta(G^*, G_k)$ or the operator bound $\sup_{\|u\| \neq 0,\, k \in \mathbb{N}_+} \frac{\|(G^*|_{u_k} - G_k) u\|}{\|u\|}$. This limits the maximum deviation that linearisation G_k can take from the true dynamics about each ILC update u_k.

Theorem 3 states that ILC stabilises a 'ball' of plants with radius $\|\Pi_{\bar{G}//\bar{C}}\|_{\bar{w}_0}^{-1}$ centred around $\bar{G}$, as shown in Fig. 5a). If the right-hand side of ILC convergence condition (8) is small, the size of the ball increases but there is a trade-off with the size of $\|L_k\|$ and $\|L_k G_k\|$. Overall robustness is dictated by the 'worst' model used in the set $\{G_k\}$. Inequality (20) then gives the resulting tracking accuracy; it bounds the plant signals from their ideal, disturbance free, values since $\|w_1 - \bar{w}_1\| \leq \|\Pi_{\bar{G}^*//\bar{C}}\|_{\bar{w}_0} \|w_0\|$.

IV. ELECTRODE ARRAY MISALIGNMENT

The largest source of error reported in clinical trials using FES arrays is due to difficulty in placing them and the resulting misalignment [36], [37]. If the wrong muscles are stimulated, the intended movement may be impossible to achieve. Its effect is so detrimental that a full re-identification of the model is often performed each time the electrode array is placed on a patient undergoing rehabilitation.

---

[1] The gap bias has been suppressed for notational simplicity.

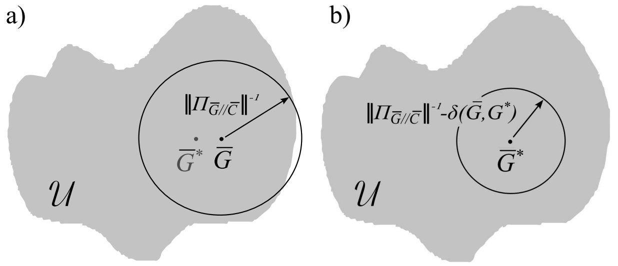

Fig. 5. a) Uncertainty space showing stability region using an ILC update designed using model $\bar{G}$ (true plant $\bar{G}^*$ must be in the circle for $[\bar{G}^*, \bar{C}]$ to be stable), b) Condition (3), Theorem 6: stability region for pure misalignment (misaligned true plant $\hat{G}$ must be in the circle).

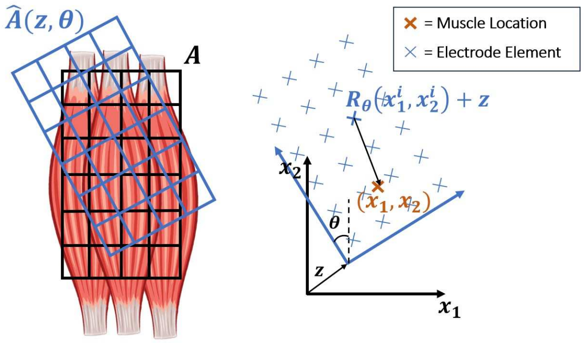

Fig. 6. (left) Array misalignment by translation z and rotation θ, with (right) corresponding geometry.

This section develops the first solution to the array misalignment control problem. To do this, the model array misalignment is modelled and its effect on robust stability is quantified. An augmented control strategy is then developed that minimises the model mismatch and thereby recovers the original nominal controller properties. The starting point is to define the effect of misalignment on the system dynamics.

Definition 5: Suppose the electrode array structure of Definition 1 is misaligned by applying a translation z and rotation θ, as shown in Fig. 6. Then the array model (1) is replaced by

$$v(t) = \hat{A}(z,\theta)u(t) \tag{22}$$

where $\hat{A}(z,\theta)$ has elements

$$\hat{A}(z,\theta)_{j,i} = \oiint_{\mathcal{M}_j} \frac{\kappa}{\|x - (R_\theta x^i + z)\|^2} dx_1 dx_2 \tag{23}$$

where $R_\theta = \begin{bmatrix} \cos\theta & -\sin\theta \\ \sin\theta & \cos\theta \end{bmatrix}$ is the 2D rotation matrix.

The following theorem computes the performance of a controller designed using model $\bar{G}$, but instead of being applied to the intended system G^* of (5), (13), it is applied to the misaligned system

$$\begin{aligned} \hat{G} &: \mathcal{U} \to \mathcal{Y} : u_1 \mapsto y_1 \\ &: y_1(k) = H_{RB} F_m H_{LAD} h_{IRC} \hat{A}(z,\theta) u_1(k). \end{aligned} \tag{24}$$

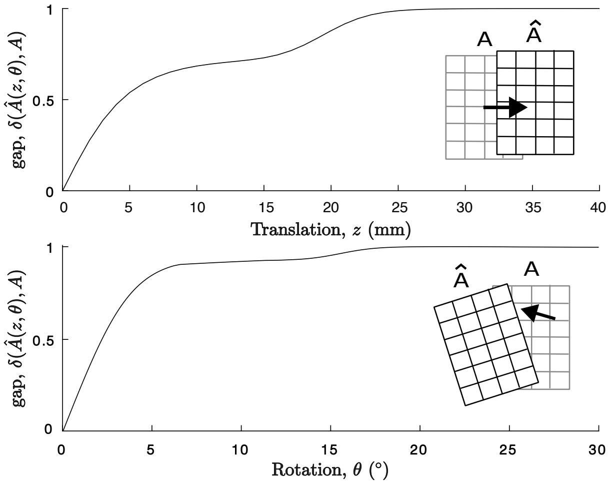

Fig. 7. Gap $\delta(\hat{A}(z,\theta),A)$ for pure horizontal translation and pure rotation alignment using the same array geometry used in clinical trials [23]. (4 × 6 array, 2cm × 1.5cm pads.

Theorem 6: Let ILC update $\bar{C}$ (14) be designed using model $\bar{G}$ (17) such that (8) holds. If it is then applied to the misaligned array system $\hat{G}$ (24), the resulting closed-loop system $[\hat{G}, \bar{C}]$ is BIBO stable if any of the following conditions hold:

(a) The gap between model and misaligned systems satisfies

$$\delta(\hat{G}, \bar{G}) < \|\Pi_{\bar{G}//\bar{C}}\|_{\bar{w}_0}^{-1}, \tag{25}$$

(b) the gap between aligned and misaligned 'true' systems satisfies

$$\delta(\hat{G}, \bar{G^*}) < \|\Pi_{\bar{G}//\bar{C}}\|_{\bar{w}_0}^{-1} - \delta(\bar{G^*}, \bar{G}), \tag{26}$$

(c) or the misaligned array geometry satisfies

$$\delta(\hat{A}(z,\theta), A) < \frac{\|\Pi_{\bar{G}//\bar{C}}\|_{\bar{w}_0}^{-1} - \delta(\bar{G^*}, \bar{G})}{\|H_{RB} F_m H_{LAD} h_{IRC}\|}. \tag{27}$$

Proof. See Appendix C. □

In all three conditions (a)-(c), the term $\|\Pi_{\bar{G}//\bar{C}}\|_{\bar{w}_0}$ can be substituted by the RHS of (19) which is readily computable. Condition (a) is the basic robustness margin of Theorem 3 but now applied to the misaligned system $\hat{G}$ instead of $\bar{G}^*$. Conditions (b) and (c) bound the misaligned and aligned systems and so directly quantify the effect of misalignment (i.e. the gaps do not involve the model). In conditions (b), (c) the term $\|\Pi_{\bar{G}//\bar{C}}\|_{\bar{w}_0}^{-1} - \delta(\bar{G^*}, \bar{G})$ represents the 'surplus robustness radius' that is available after the ILC update is applied to the aligned true plant G^*. This defines the maximum misalignment that can be tolerated, and is illustrated in Fig. 5b). In practical terms, if the ILC controller is robust and/or the model $\bar{G}$ is close to the aligned system $\bar{G}^*$, then there is more margin available to accommodate misalignment. The tracking accuracy of the misaligned system can be computed by (20) with G^* replaced by $\hat{G}$.

Theorem 6 shows that the stability and tracking performance of controller C degrades as the misalignment increases. To illustrate this, Fig. 7 shows plots of $\delta(\hat{A}, A)$ for ranges of array rotation and translation that typically occur in FES experiments with stroke patients [37] and unimpaired participants [36]. It is obvious that the gap approaches its maximum of 1 with only small amounts of misalignment.

A. Realignment Controller

If the array misalignment (θ, z) is known, it is possible to adjust the FES control signal to correct for it. The next result addresses this by expanding the control action to ameliorate the effect of misalignment and recover robust stability bounds.

Theorem 7: Let ILC update $\bar{C}$ (14) be designed for an aligned true plant using model $\bar{G}$ such that convergence condition (8) holds. Suppose the true plant is then misaligned, but the ILC update is modified to the form

$$\begin{aligned} \bar{C} : \mathcal{Y} \to \mathcal{U} : y_2 \mapsto u_2 : u_2(k) &= T(z,\theta)v(k), \\ v(k+1) &= v(k) + L_k y_2(k) \end{aligned} \tag{28}$$

where

$$T(z,\theta) := \hat{A}^{\dagger}(z,\theta)A \tag{29}$$

is a 'realignment' mapping. In this case the misaligned system $[\hat{G}, \bar{C}]$ is stable if any of the conditions (a)-(c) in Theorem 6 hold, but with $\delta(\hat{G}, \bar{G})$ replaced by $\delta(\hat{G}T(z,\theta), \bar{G})$ and $\delta(\hat{A}(z,\theta), A)$ replaced by $\delta(\hat{A}(z,\theta)T(z,\theta), A)$. Moreover, the form (29) minimises both these gaps, i.e. T is the optimiser

$$\min_{T \in \mathbb{R}^{l \times n}} \delta(\hat{G}T(z,\theta), \bar{G}) \quad \text{and} \quad \min_{T \in \mathbb{R}^{l \times n}} \delta(\hat{A}(z,\theta)T(z,\theta), A) \tag{30}$$

and hence maximises the robust stability bounds. Finally, the choice (29) also maximises the tracking accuracy.

Proof: See Appendix D. □

The update (28) comprises two parts: The first is exactly the same standard ILC algorithm as previously employed in (14) which uses the tracking error y_2 to update the control action. The second is the mapping $T(z,\theta)$, which is applied to the ILC control action in order to correct for the misalignment, e.g. if the array was physically misaligned by 1cm (z = 1cm), then the mapping implements (as closely as possible) a shift in the FES pattern of -1cm to correct for it.

Unfortunately the realignment operator $T(z,\theta)$ requires knowledge of the misalignment which is typically unknown as it is caused by inevitable day-to-day variation in placement by patients or carers. This issue will be solved in the next section, by using controller (28) within a multiple model structure. By designing models with a variety of different misalignment (values of z, θ), the framework will automatically choose the most appropriate based on previous data. Therefore exact knowledge of the misalignment will no longer be required.

V. EMMILC STRUCTURE

EMMILC was introduced in [25] and builds on the multiple model switched adaptive control (MMSAC) framework of [38]. This section applies it to the FES array system defined in Section II-A. The EMMILC architecture first requires that a set of m candidate plant models $\mathcal{G} = \{\bar{G}_1, \ldots, \bar{G}_m\}$ is designed with associated candidate ILC controllers $\mathcal{C} = \{\bar{C}_1, \ldots, \bar{C}_m\}$. Each model has form (17) and is mapped to a controller of form (28) by the control design operator $K : \bar{G}_i \to \bar{C}_i$. Switching between controllers is determined using a bank of estimators, $\mathcal{X} = \{X_1, \ldots, X_m\}$, which compute a residual for each plant model in $\mathcal{G}$. Each residual measures how closely a particular model matches the measured signals (u_2, y_2), and the controller corresponding to the model with smallest residual is switched into closed-loop. Fig. 8 shows the overall structure.

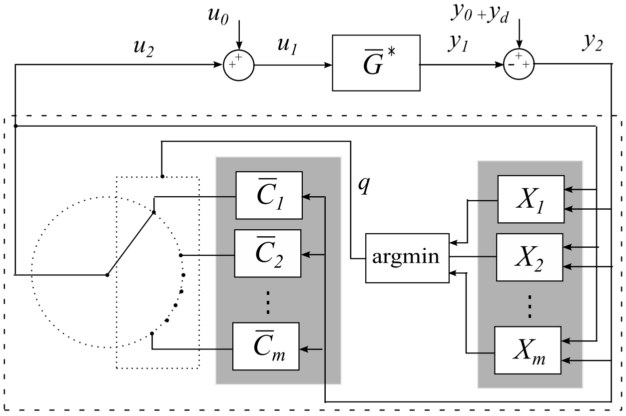

Fig. 8. EMMILC block diagram showing true plant $\bar{G}^*$, controller set $\{\bar{C}_i\}$, estimator bank $\{X_i\}$, with closed-loop $[\bar{G}^*, K(G_q)]$, $q(k) := \arg\min_i r_i^{\lambda}(k)$.

Based on the underlying theory in [25], there are two conditions that must be satisfied to guarantee stability of the EMMILC system:

(i) **Estimator granularity**

$$\exists\ \bar{G}_i \in \mathcal{G}, \quad s.t. \quad \delta(\bar{G}^*, \bar{G}_i) < \rho(\mathcal{G}, \mathcal{C}, \mathcal{U}), \tag{31}$$

(ii) **Stabilisation of uncertainty space**

$$\exists\ \bar{C}_i \in \mathcal{C}, \quad s.t. \quad \|\Pi_{\bar{G}//\bar{C}_i}\|_{\bar{w}_0} < \infty \quad \forall \bar{G} \in \mathcal{U}, \tag{32}$$

where $\rho(\cdot)$ is defined explicitly in [25]. These ensure that the models $\{\bar{G}_1, \ldots, \bar{G}_m\}$ are sufficiently close together, and that there exists at least one controller within the set $\mathcal{C}$ able to stabilise any plant within the uncertainty space, as illustrated in Fig. 9.

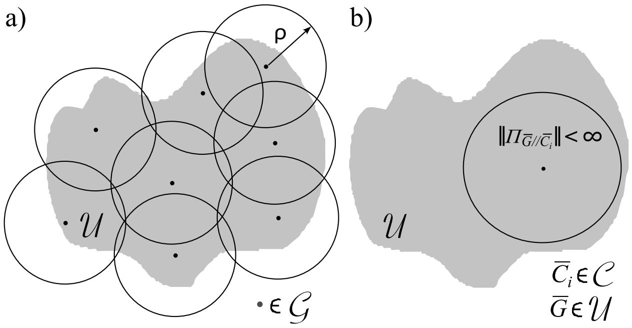

Fig. 9. EMMILC conditions: a) Uncertainty set $\mathcal{U}$ covered by gap balls of radius ρ. b) For every plant $\bar{G} \in \mathcal{U}$ there exists a stabilising controller $\bar{C}_i \in \mathcal{C}$.

Condition (ii) is readily verified by applying Theorem 3 to each controller in $\mathcal{C}$, and the gap measurement in condition (i) can be computed using (21). If these hold, then the tracking error is bounded as

$$\|w_2\|_{\bar{w}_2} < \eta(\mathcal{G}, \mathcal{C}, \mathcal{U}) \tag{33}$$

where $\eta(\cdot)$ is defined in [25].

A. Estimator design

EMMILC supports either infinite or finite horizon estimators, both encompassed by the general form $X_i^\lambda : (u_2, y_2)^\top \rightarrow r_i^\lambda$, which computes the size of the smallest disturbance estimate (u_0, y_0) needed to explain the observed signals (u_2, y_2) over trial horizon $[k-\lambda, k]$ under the assumption that model $\bar{G}_i$ is the true plant. Let $\mathcal{N}_i^{[a,b]}(u_2, y_2)$ be the set of all possible disturbances compatible with $\bar{G}_i$ and observed signals $(u_2(k), y_2(k))$ over trial $a, a+1, \ldots, b$. Then the residual for model $\bar{G}_i$ is computed as

$$r_i^\lambda(k) := \inf_{w_0}\{r \geq 0 \mid r = \|w_0\|, \ w_0 \in \mathcal{N}_i^{[k-\lambda,k]}(u_2, y_2)\} \tag{34}$$

The next theorem shows how this can be computed for both finite and infinite horizon cases, and provides a computationally tractable implementation.

Theorem 8: Residual computation (34) is solved recursively for the infinite horizon case by

$$r_i^k(k) = \|r_i^{k-1}(k-1), r_i^0(k)\|, \quad r_i^0(0) = 0, \tag{35}$$

and for the finite horizon case by

$$r_i^\lambda(k) = \sqrt{\sum_{j=0}^{\lambda} (r_i^0(k-j))^2} \tag{36}$$

where the residual calculation for only trial k is

$$r_i^0(k) = \inf_{w_0}\{r \geq 0 \mid r = \|w_0\|, \ w_0 \in \mathcal{N}_i^{[k,k]}(u_2, y_2)\}. \tag{37}$$

If the lifted candidate model $\bar{G}_i$ has unlifted form realised on trial k by the discrete state-space triple $\{A_i(t), B_i(t), C_i(t)\}$, running over $t = 0, \cdots, N$, then residual (37) can be computed as

$$r_i^0(k) = \left[\sum_{t=0}^{N} \|y_d(t) - e_k(t) - C_i(t)\hat{x}(t)\|^2_{[C_i(t)\Sigma(t)C_i(t)^\top + I]^{-1}}\right]^{\frac{1}{2}} \tag{38}$$

with $\hat{x}(t)$ generated by the extended Kalman filter system

$$\begin{aligned} \hat{x}(t+1/2) &= \hat{x}(t) + \Sigma(t)C_i(t)^\top[C_i(t)\Sigma(t)C_i(t)^\top + I]^{-1} \\ &\qquad \cdot [y_d(t) - e_k(t) - C_i(t)\hat{x}(t)] \qquad (39) \\ \Sigma(t+1/2) &= \Sigma(t) - \Sigma(t)C_i(t)^\top[C_i(t)\Sigma(t)C_i(t)^\top + I]^{-1} \\ &\qquad \cdot C_i(t)\Sigma(t) \qquad (40) \\ \hat{x}(t+1) &= A_i(t)\hat{x}(t+1/2) + B_i(t)v_k(t) \qquad (41) \\ \Sigma(t+1) &= A_i(t)\Sigma(t+1/2)A_i(t)^\top + B_i(t)B_i(t)^\top, \qquad (42) \end{aligned}$$

where $\hat{x}(0) = 0$, $\Sigma(0) = B_i(0)B_i(0)^\top$.
Proof This follows from [38] and the deterministic interpretation of the Kalman Filter, see e.g. [39], [40]. □

B. EMMILC design procedure

To satisfy EMMILC condition (ii) using Theorem 3 means selecting a set of candidate models $\{\bar{G}_i\}$ with corresponding controllers $\{\bar{C}_i\}$, and then ensuring that the union of their gap balls (center $\bar{G}_i$, radius $\|\Pi_{\bar{G}_i//\bar{C}_i}\|^{-1}_{\bar{w}_0}$) covers the uncertainty space $\mathcal{U}$. Condition (i) is similar, but imposes an upper limit on the minimum distance between each candidate model. To simplify the two conditions, they can be combined into a single condition:

$$\exists\, \bar{G}_i \in \mathcal{G} \ \ s.t. \ \ \delta(\bar{G}^*, \bar{G}_i) < \alpha\|\Pi_{\bar{G}_i//\bar{C}_i}\|^{-1}_{\bar{w}_0} \ \ \forall \bar{G}^* \in \mathcal{U} \tag{43}$$

where $0 < \alpha \leq 1$ is a tunable gain chosen by the designer. When $\alpha = 1$, this satisfies condition (ii) as it states that the gap balls must cover $\mathcal{U}$ and have a maximum radius of $\|\Pi_{\bar{G}_i//\bar{C}_i}\|^{-1}_{\bar{w}_0}$. Reducing α shrinks the radius of the gap balls, requiring more, closely packs balls. As the plant models become closer and closer, there will always come a point at which condition (i) will be satisfied. This means there is no need to calculate ρ, and instead the designer may treat α as a tunable gain.

Based on this approach, practical implementation of the EMMILC framework can be summarised as follows.

1) **Model structure:** Determine a suitable structure of components H_{RB}, F_m, H_{LAD}, h_{IRC}, A in (5) to represent the true plant G^*.
2) **Uncertainty space $\mathcal{U}$:** Identify a minimum range of model parameters necessary to capture the possible variation in the true plant dynamics. For the case of array misalignment this will be the union of all possible values of shift z and rotation θ.
3) **Controller design procedure:** Select a suitable type of ILC update law (7) for use in the candidate controllers (28). This should balance robustness (measured by (18)) with convergence (measured by the RHS of (8)).
4) **Model set $\mathcal{G}$:** Construct a model set $\mathcal{G}$ which satisfies (43) for $0 \leq \alpha \leq 1$. Smaller values of α will improve robust performance but will have a higher computational cost due to an increased number of candidate plant models.
5) **Estimator set:** For each model, implement estimator X_i^λ using (35) or (36). Select λ to balance sensitivity against adaptability to changing dynamics.
6) **Check performance:** Apply EMMILC in practice and if performance is unsatisfactory reduce the value of α in Step 4).

VI. NUMERICAL RESULTS

The approach is now applied to a realistic simulation of the human hand [41]. The model contains $l = 6$ muscles, namely the extensor communis (EC), extensor carpi radialis brevis (ECRB), extensor indicis (EI), extensor carpi ulnaris (ECU), flexor digitorum profundus (FDP), and flexor digitorum superficialis (FDS). The $q = 2$ outputs comprise the wrist and metacarpophalangeal (MCP) joints. Stimulation is applied using a 8×6 element electrode array, giving a total of $n = 48$ elements. The pad dimensions of 2cm × 1.5cm match those used clinically [15], and combine with neuromuscular junction positions to give array operator A. The h_{IRC} form was chosen as

$$w_j = a_1 \frac{e^{a_2 v_j} - 1}{e^{a_2 v_j} + a_3}. \tag{44}$$

which accurately captures muscle dynamics using parameters $a_1, a_2, a_3 \in \mathbb{R}$ [28]. Operators $H_{LAD,j}$ were modelled as second order, critically damped systems with natural frequency ω_n. The forms of $M(y)$, $C(y, \dot{y})$, and $K(y)$ matched those given in [29], [42].

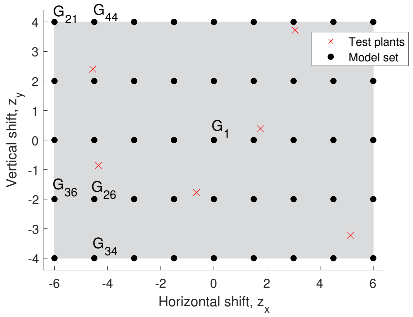

Fig. 10. Uncertainty space, candidate model set $\mathcal{G}$ distribution, and location of true plants (indicated by red crosses).

Simulations took u_0, y_0 as white Gaussian noise with a signal-to-noise ratio of 30 in order to replicate previous clinical trials [37]. The reference was chosen as $y_{d,1} = 66°$, $y_{d,2} = 53°$ to correspond to a pinch posture [15].

A. EMMILC Design

After establishing the model structure, the next step is to define the uncertainty space $\mathcal{U}$. The investigation focuses on whether EMMILC can address the array misalignment problem, and therefore the uncertainty is restricted to only array misalignment parameters. This enables clearer conclusions to be drawn that do not involve other, less destabilising, sources of uncertainty (fatigue, spasticity etc) which will be investigated separately. Translational uncertainty was considered, with a horizontal misalignment range between -6cm and +6cm, and vertical misalignment range between -4cm and +4cm. Hence the parameterised uncertainty space is $\mathcal{U} := \{\hat{G} \text{ given by } (24) \mid z = (z_x, z_y),\ z_x \in [-6, 6],\ z_y \in [-4, 4]\}$.

From (28), the control design procedure, K, maps each $\bar{G}_i \in \mathcal{G}$ to

$$\begin{aligned} \bar{C}_i : \mathcal{Y} \to \mathcal{U} : y_2 \mapsto u_2 : u_2(k) = T(z,\theta)v(k), \\ v(k+1) = v(k) + L_{k,i} y_2(k). \end{aligned} \tag{45}$$

Gradient ILC was selected due to its favourable robustness properties, so that learning operator $L_{k,i} = \gamma(G_{k,i})^\top$ with γ a scalar design parameter. Realignment matrix $T(z,\theta)$ is defined by the form (29).

For the estimator design, the infinite horizon case was selected and was computed using (35). Preliminary tests were carried out in which EMMILC design parameter γ was tuned heuristically to ensure robust convergence within 30 trials. This was achieved using $\gamma = 10,000$. Parameter α in (43) was tuned to give a high density of distinct models. The resulting model set distribution is shown in Fig. 10.

Six different misaligned plants were then generated, to examine the effectiveness of the proposed controller. These plants were spread evenly across the uncertainty spaces; their distribution is also shown in Fig. 10.

B. Results

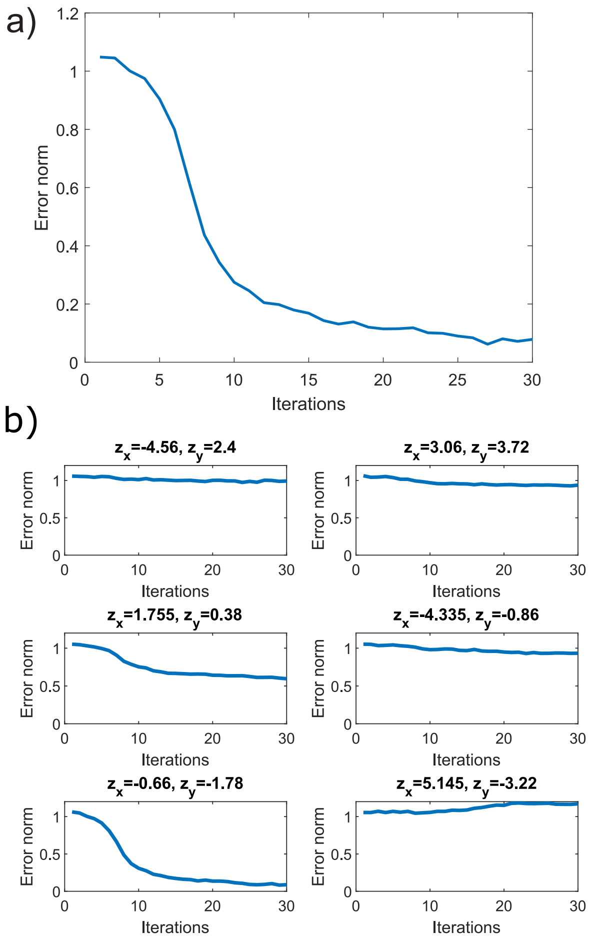

Fig. 11. Standard ILC applied with a) perfect alignment, and b) six different misalignment.

First results using standard ILC are shown. Standard ILC is the only existing model based controller to have been applied to FES electrode arrays, and so is the obvious comparison with EMMILC. Update (14) was applied to the true plant, with $L_k = \gamma(G_k)^\top$, where G_k is the local linearisation of the true plant dynamics (i.e. $G^*|_{u_k}$). Fig. 11a) shows that the ILC error norm converges close to the desired reference. This result assumed exact plant knowledge (i.e. perfect array alignment). To investigate the effect of misalignment, the A matrix (2) in the true plant model was exchanged for the misaligned form $\hat{A}(z,\theta)$ (23). The model used by the ILC update was unchanged. When the array was shifted the performance using the inaccurate model rapidly degraded, as shown in Fig. 11b). This shows the performance for the six misalignment cases shown by red crosses in Fig. 10, and reveals that in many cases the converged error norm is much larger than when the array is perfectly aligned, and in one case can be seen to diverge. The average error norm over the final five trials is 0.788, compared to 0.078 when considering perfect alignment.

Fig. 12a) shows the convergence when EMMILC is used to control the same six misaligned array cases. Using EMMILC, each of the cases converges to a consistently smaller error norm than when using standard ILC. The mean converged error norm using EMMILC is 0.086, 89% less than that the value obtained with standard ILC, and comparable to the

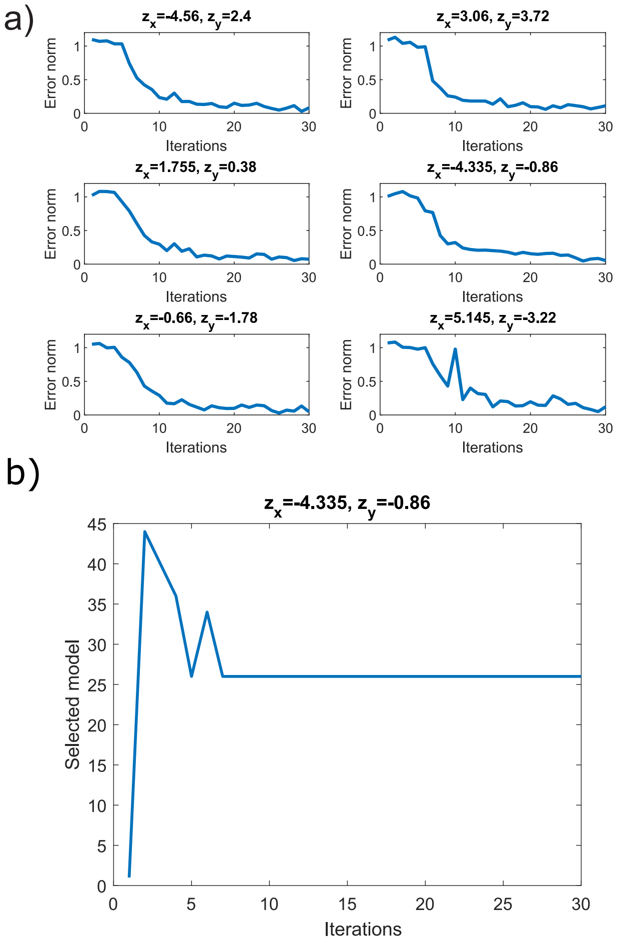

Fig. 12. EMMILC a) performance and b) example of switching signal q for EMMILC with array misalignment.

performance with perfect array alignment (i.e. Fig. 11a)). An example of the model switching signal is shown in Fig. 12b), confirming that EMMILC converges to the optimal model within seven trials. The next section extends these results by evaluating EMMILC experimentally.

VII. EXPERIMENTAL RESULTS

The hardware comprises a depth camera (Leap Motion Controller 2, Ultraleap), user interface software running on a laptop, a real-time controller running on a Raspberry Pi 4, and a 64 channel FES electrode array and electronics embedded in a sleeve. Data are transmitted via wi-fi and the real-time controller runs at 40 Hz. The frequency and amplitude of each pulse train are fixed, and the pulse width of each pulse train is the controlled variable (0 - 300 μs). The components are shown in Fig. 13 and described further in [43]. The choice of joint angles (wrist, MCP) and task (pinch posture) match those of Section VI.

EMMILC will again be compared with standard ILC, as the only existing model based controller. It will also be compared against the sequential open-loop control of each pad, used in [17]–[19], which mimics manual application by a physiotherapist and is the most prevalent control approach for FES arrays. Each controller will be applied with varying degrees of array misalignment. For ILC, the mean error norm over the last five iterations will again be taken.

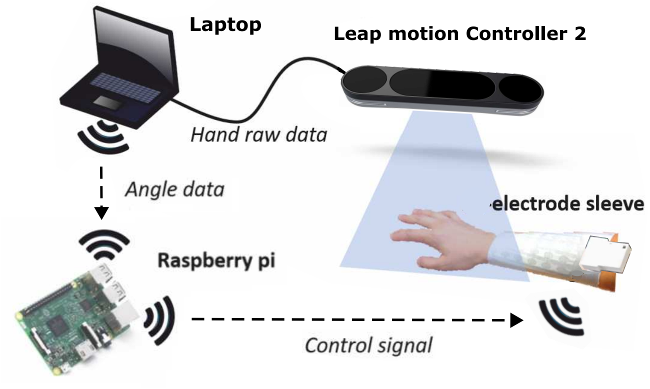

Fig. 13. Upper limb stroke rehabilitation hardware.

A. Control Design

Control design mirrors Section VI, but with the addition of tests to identify muscle locations and a nominal model. The procedure is as follows:

(i) Sequential open-loop control involves applying a 10 second ramp input to each array element and then measuring the resulting joint motion. To locate the dominant muscle locations, the two array elements, i_1, i_2, that produce the most movement of one angle, and least of the other, are selected. The optimum stimulation level for each one is then computed to best attain the specified pinch reference.

(ii) Standard ILC follows the same design as in Section VI. Model structure $H_{RB}H_{LAD}h_{IRC}$ is fitted to the i_1, i_2 pad ramp responses, with component $H_{LAD,j}$ again selected as a critically damped system, $h_{IRC,j}$ as a constant gain, and $H_{RB}(s) = \frac{1}{I_s s^2 + B_s s + K_s}$ is chosen to match [26].

(iii) EMMILC uses the above model structure for each candidate model, but adds the array misalignment term $\hat{A}(z, \theta)$ specified in (24). The same misalignment uncertainty set as in Section VI is applied which is sampled to produce 45 candidate models, each with an associated realignment controller (45). Estimator design follows the approach of Section VI.

B. Results

Ethics approval was granted by University of Southampton Ethics and Research Governance Online (ERGO), ID 102462. Three unimpaired subjects were recruited, as a prerequisite for later clinical tests with stroke patients.

Results for the sequential open-loop and standard ILC approaches are shown in Fig. 14 for one participant and those for EMMILC are in Fig. 15. Seven different array alignments were tested, with misalignments ranging between $z_x = \pm$ 3cm and $z_y = \pm$ 2cm. The mean error norm over all alignment conditions and all participants for sequential control is 0.668. Likewise, the mean error norm over the last five trials of

TABLE I
ERROR NORM RESULTS FOR THREE CONTROLLERS ((I) SEQUENTIAL OPEN-LOOP, (II) STANDARD ILC, (III) EMMILC) AND SEVEN DIFFERENT MISALIGNMENT CONDITIONS (z_x, z_y).

	Array alignment, (z_x, z_y)						
	$(3, 2)$	$(1.5, 0)$	$(3, -2)$	$(-3, -2)$	$(-1.5, 0)$	$(-3, 2)$	$(0, 0)$
(i) P1	0.934	0.601	0.870	0.673	0.624	0.941	0.249
P2	0.840	0.541	0.681	0.776	0.564	0.773	0.311
P3	0.836	0.652	0.836	0.711	0.573	0.810	0.228
(ii)P1	0.802	0.386	0.851	0.667	0.533	0.760	0.149
P2	0.766	0.411	0.781	0.731	0.509	0.871	0.128
P3	0.921	0.456	0.790	0.821	0.672	0.788	0.179
(iii)P1	0.201	0.223	0.241	0.292	0.300	0.331	0.131
P2	0.156	0.121	0.197	0.179	0.167	0.196	0.118
P3	0.178	0.134	0.156	0.201	0.198	0.241	0.104
95% CI	[0.597, 0.786]	[0.049, 0.467]	[0.547, 0.671]	[0.201, 0.829]	[0.049, 0.649]	[0.245, 0.856]	[-0.053, 0.122]
p-value	0.001	0.009	0.009	0.016	0.003	0.000	0.026

standard ILC is 0.618. The mean error norm over the last five trials of EMMILC is 0.194. This is 71.0% less than sequential control, and 68.7% less than standard ILC.

A paired sample t-test was performed to test whether the reduced error norm produced by EMMILC was significant compared with standard ILC. The '95% CI' row denotes the 95% confidence interval of the difference in error norms for each alignment, and corresponding p-values are given. Significant results are highlighted in green. These confirm that the improvement of EMMILC is significant in all misalignment scenarios. The improvement compared with sequential open-loop control are not shown, but are also all significant.

Compared with the numerical results of Section VI, the accuracy is degraded due to the simple model structure used and physiological variation. This could be addressed by adding uncertainty sets for physiological parameters. Note that EMMILC only requires a single session for design and then does not require any tuning or identification tests to maintain high accuracy. This contrasts with the other controllers that would require the identification procedure to be repeated on subsequent sessions to maintain high accuracy. This process takes over 10 minutes and requires a control engineer, making it infeasible for clinical or home use. The results therefore establish the potential of EMMILC to provide effective rehabilitation in the home, and lay the foundation for clinical trials.

VIII. CONCLUSIONS AND FUTURE WORK

A solution to the control of FES electrode arrays for hand and wrist rehabilitation has been developed. This integrates a comprehensive model, a novel realignment controller to maximise robust performance, and an extension to multiple-model switched ILC. The effectiveness of the overall EMMILC approach compared with the leading alternatives was demonstrated using both realistic simulations and experiments.

The results have provided the necessary foundation on which to conduct experimental tests with stroke patients. Therefore future work will involve running a clinical feasibility study with 5-10 neurologically impaired participants.

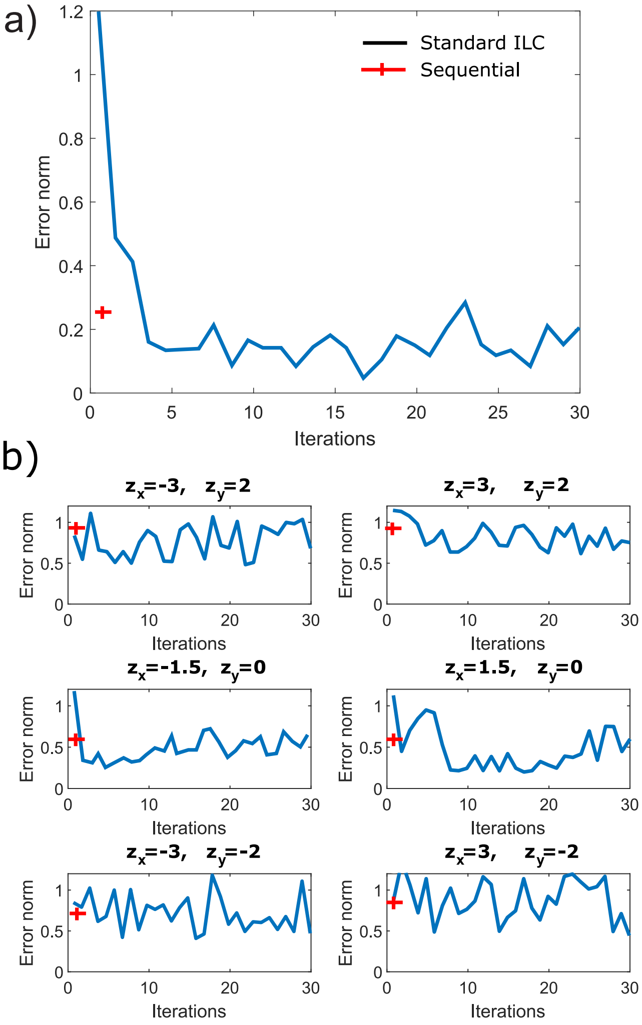

Fig. 14. Sequential and standard ILC error norm results for participant P1, with a) perfect alignment, and b) six different misalignments.

APPENDIX A
PROOF OF DEFINITIONS 1 AND 5

The overall charge contribution of the i^{th} electrode is modelled as a point charge q_i applied at its centre (x_i, y_i), which generates an electric field whose strength at a point (x_j, y_j) is dictated by Coulomb's law

$$E_i(x_j, y_j) = \frac{\kappa}{r^2_{i,(x_j,y_j)}} q_i \tag{46}$$

where $\kappa \approx 8.99 \times 10^9 Nm^2C^{-2}$ and $r_{i,(x_j,y_j)}$ is the distance between (x_j, y_j) and (x_i, y_i) [44]. Due to the principal of charge superposition, the total electric field strength experienced by muscle j is

$$v(t) = \sum_{i=1}^{n} \oiint_{\mathcal{M}_j} E_i(x, y) dx dy. \tag{47}$$

Denote each element of A as (2) and set $u_i = q_i$ to get (1).

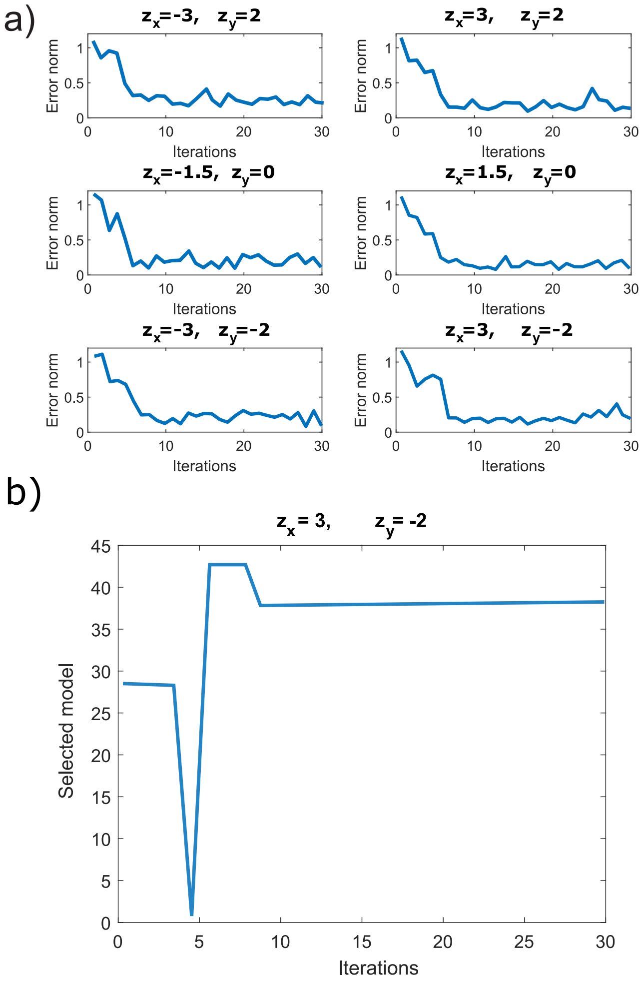

Fig. 15. EMMILC error norm results for participant P1, showing a) performance for different misalignments and b) example of switching signal q.

APPENDIX B
PROOF OF THEOREM 3

From (14) and the Fig. 4 relations

$$\begin{aligned} u_2(k+1) &= u_2(k) + L_k(y_0(k) + y_d - G_k(u_0(k) + u_2(k)) \\ &= (I - L_kG_k)u_2(k) + L_k(y_0(k) + y_d - G_ku_0(k)) \end{aligned}$$

Since $u_2(0) = 0$, this gives rise to the recurrent relation

$$u_2(k) = \sum_{i=1}^{k} Z^k_{k-i}L_{k-i}(y_0(k-i) + y_d - G_{k-i}u_0(k-i))$$

where $Z^b_a = \prod_{n=a+1}^{b-1}(I - L_nG_n)$. It follows that

$$\begin{aligned} u_1(k) =& u_0(k) + \sum_{i=1}^{k} Z^k_{k-i}L_{k-i}(y_0(k-i) + y_d - \\ & G_{k-i}u_0(k-i)) \end{aligned} \tag{48}$$

and so the projection operators are

$$\left(\Pi_{\bar{G}//\bar{C}}\bar{w}_0\right)(k) = \begin{pmatrix} I \\ G_k \end{pmatrix} \sum_{i=1}^{k} Z^k_{k-i}L_{k-i}y_d, \tag{49}$$

$$\begin{aligned} &\left(\Pi_{\bar{G}//\bar{C}}(w_0+\bar{w}_0)\right)(k) = \begin{pmatrix} I \\ G_k \end{pmatrix}\Big(u_0(k) + \\ &\sum_{i=1}^{k} Z^k_{k-i}L_{k-i}(y_0(k-i) + y_d - G_{k-i}u_0(k-i))\Big) \end{aligned} \tag{50}$$

and the biased norm equation is then

$$\begin{aligned} &\left\|\Pi_{\bar{G}//\bar{C}}\right\|_{\bar{w}_0} \\ &= \sup_{\|w_0\|\neq 0} \frac{\sup_{0\leq k\leq\infty}\left\| \begin{matrix}\left(\Pi_{\bar{G}//\bar{C}}(w_0+\bar{w}_0)\right)(k) - \\ \left(\Pi_{\bar{G}//\bar{C}}\bar{w}_0\right)(k)\end{matrix} \right\|}{\sup_{0\leq k\leq\infty}\|w_0(k)\|} \\ &= \sup_{\|w_0\|\neq 0} \frac{\sup_{0\leq k\leq\infty}\left\| \begin{pmatrix} I \\ G_k \end{pmatrix} \begin{pmatrix} \sum_{i=1}^{k} Z^k_{k-i}L_{k-i}(y_0(k-i) - \\ G_{k-i})u_0(k-i) + u_0(k) \end{pmatrix} \right\|}{\sup_{0\leq k\leq\infty}\|w_0(k)\|} \end{aligned} \tag{51}$$

To bound the operator, use the result that

$$\left\|\Pi_{\bar{G}//\bar{C}}\right\|_{\bar{w}_0} \leq \|\Pi_{\bar{G}//\bar{C}}|_{y_0=0}\|_{\bar{w}_0} + \|\Pi_{\bar{G}//\bar{C}}|_{u_0=0}\|_{\bar{w}_0}. \tag{52}$$

The first term on the right-hand side is bounded as

$$\begin{aligned} &\left\|\Pi_{\bar{G}//\bar{C}}\begin{pmatrix} 0 \\ y_0 \end{pmatrix}\right\|_{\bar{w}_0} \\ &= \sup_{0\leq k\leq\infty}\left\|\begin{pmatrix} I \\ G_k \end{pmatrix}\sum_{i=1}^{k} Z^k_{k-i}L_{k-i}y_0(k-i)\right\| \\ &= \sup_{0\leq k\leq\infty}\sum_{i=1}^{k}\left\|\begin{pmatrix} I \\ G_k \end{pmatrix} Z^k_{k-i}L_{k-i}y_0(k-i)\right\| \\ &\leq \sup_{0\leq k\leq\infty}\sum_{i=1}^{k}\left(\left\|\begin{pmatrix} I \\ G_k \end{pmatrix} Z^k_{k-i}L_{k-i}\right\| \|y_0(k-i)\|\right) \\ &\leq \left(\sup_{0\leq k\leq\infty}\sum_{i=1}^{k}\left\|\begin{pmatrix} I \\ G_k \end{pmatrix} Z^k_{k-i}L_{k-i}\right\|\right) \sup_{0\leq k\leq\infty}\|y_0(k)\| \\ &\leq \left(\lim_{k\to\infty}\sum_{i=1}^{k}\left\|\begin{pmatrix} I \\ G_k \end{pmatrix} Z^k_{k-i}L_{k-i}\right\|\right) \sup_{0\leq k\leq\infty}\|y_0(k)\| \\ &\leq \sup_{0\leq k\leq\infty}\left\|\begin{pmatrix} I \\ G_k \end{pmatrix}\right\|\|L_{k-i}\| \left(\lim_{k\to\infty}\sum_{i=1}^{k}\|Z^k_{k-i}\|\right) \times \\ &\qquad \sup_{0\leq k\leq\infty}\left\|y_0(k)\right\|. \end{aligned}$$

Then since $\|I - L_jG_j\| < 1$

$$\lim_{k\to\infty}\sum_{i=1}^{k}\|Z^k_{k-i}\| \leq \frac{1}{1 - \sup_{0\leq k\leq\infty}\|I - L_kG_k\|} \tag{53}$$

it follows that

$$\begin{aligned} &\|\Pi_{\bar{G}//\bar{C}}|_{y_0=0}\|_{\bar{w}_0} \\ &\leq \frac{\sup_{0\leq k\leq\infty}\left\|\begin{pmatrix} I \\ G_k \end{pmatrix}\right\| \sup_{0\leq k\leq\infty}\|L_k\|}{1 - \sup_{0\leq k\leq\infty}\|I - L_kG_k\|} \end{aligned} \tag{54}$$

Repeating for $y_0 = 0$:

$$\left\|\Pi_{\bar{G}//\bar{C}}\binom{u_0}{0}\right\|_{\bar{w}_0}$$

$$= \sup_{0\le k\le\infty}\left\|\binom{I}{G_k}\Big(u_0(k) - \sum_{i=1}^{k} Z^k_{k-i}L_{k-i}G_{k-i}u_0(k-i)\Big)\right\|$$

$$\le \sup_{0\le k\le\infty}\left\|\binom{I}{G_k}\left(\sum_{i=1}^{k} Z^k_{k-i}L_{k-i}G_{k-i}u_0(k-i)\right)\right\| +$$

$$\sup_{0\le k\le\infty}\left\|\binom{I}{G_k}u_0(k)\right\|.$$

Proceeding as before, this results in

$$\|\Pi_{\bar{G}//\bar{C}}|_{u_0=0}\|_{\bar{w}_0}$$

$$\le \frac{\sup\limits_{0\le k\le\infty}\left\|\binom{I}{G_k}\right\| \sup\limits_{0\le k\le\infty}\|L_kG_k\|}{1-\sup\limits_{0\le k\le\infty}\|I-L_kG_k\|} + \sup_{0\le k\le\infty}\left\|\binom{I}{G_k}\right\|.$$

Substituting this and (54) into (52) yields the final bound

$$\left\|\Pi_{\bar{G}//\bar{C}}\right\|_{\bar{w}_0} \le \sup_{0\le k\le\infty}\left\|\binom{I}{G_k}\right\|\left(1+ \frac{\sup_{0\le k\le\infty}\left(\|L_k\|+\|L_kG_k\|\right)}{1-\sup_{0\le k\le\infty}\|I-L_kG_k\|}\right). \tag{55}$$

APPENDIX C
PROOF OF THEOREM 6

Replacing $\bar{G}^*$ with $\hat{G}$ in (18) yields (25), and (26) follows from the triangle inequality, i.e.

$$\delta(\hat{G},\bar{G}) \le \delta(\bar{G}^*,\bar{G}) + \delta(\hat{G},\bar{G}^*). \tag{56}$$

Then bound the 'true system' gap using its definition

$$\delta(\hat{G},\bar{G}^*) := \inf_{\Psi\in Q}\ \sup_{\substack{x\neq 0\\ x\in \mathrm{dom}(\hat{\mathcal{G}})}} \frac{\|(\Psi-I)x\|}{\|x\|} \tag{57}$$

$$\le \inf_{\Upsilon\in\Omega}\ \sup_{\substack{x\neq 0\\ x\in \mathrm{dom}(\hat{\mathcal{G}})}} \frac{\left\|\begin{pmatrix} I & 0\\ 0 & H_{RB}F_mH_{LAD}h_{IRC}\end{pmatrix}(\Upsilon-I)x\right\|}{\|x\|}$$

$$\le \inf_{\Upsilon\in\Omega}\left\|\begin{pmatrix} I & 0\\ 0 & H_{RB}F_mH_{LAD}h_{IRC}\end{pmatrix}\right\| \sup_{\substack{u\neq 0\\ u\in \mathrm{dom}(\hat{G})}}\frac{\|(\Upsilon-I)u\|}{\|u\|}$$

$$\le \|H_{RB}F_mH_{LAD}h_{IRC}\|\delta(\hat{A},A) \tag{58}$$

in which the set of operators $Q := \{\Psi : \hat{\mathcal{G}} \mapsto \bar{\mathcal{G}}^*\}$, and $\Omega := \{\Upsilon : \hat{\mathcal{A}} \mapsto \mathcal{A}\}$ where $\hat{\mathcal{A}}$ is the graph of $\hat{A}(z,\theta)$ and $\mathcal{A}$ is the graph of A. Similarly, the graphs $\bar{\mathcal{G}}^* := \left\{\begin{pmatrix} u_1\\ y_1\end{pmatrix} : y_1 = \bar{G}^*u_1, u_1 \in \mathcal{U}\right\}$, $\hat{\mathcal{G}} := \left\{\begin{pmatrix} u_1\\ y_1\end{pmatrix} : y_1 = \hat{G}u_1, u_1 \in \mathcal{U}\right\}$. Substituting (58) into (56) and rearranging yields (27).

APPENDIX D
PROOF OF THEOREM 7

Fig. 16a) shows the controller form (28) inserted into Fig. 4 with $\hat{G}$ as the true plant. The aim is to establish conditions for stability of this system, given that $\bar{C}$ is designed to stabilise $\bar{G}$, as shown in Fig. 16b). First rearrange the systems of Fig. 16 to the form of Fig. 17, where $u_{0,2}$ is an addition disturbance. Stability of Fig. 17a) guarantees stability of Fig. 16a) (since it is the special case $u_{0,2} = 0$). Now apply gap-based stability analysis to the Fig. 17 augmented systems. The nominal model of Fig. 17b) has projection operator

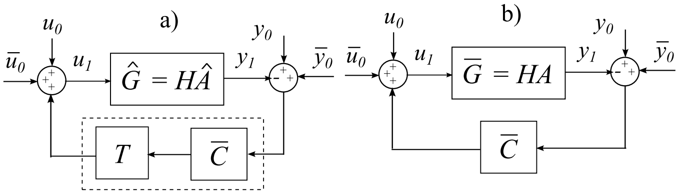

Fig. 16. ILC configurations: a) misaligned plant and controller (28), b) aligned plant with controller (14) designed to stabilise it.

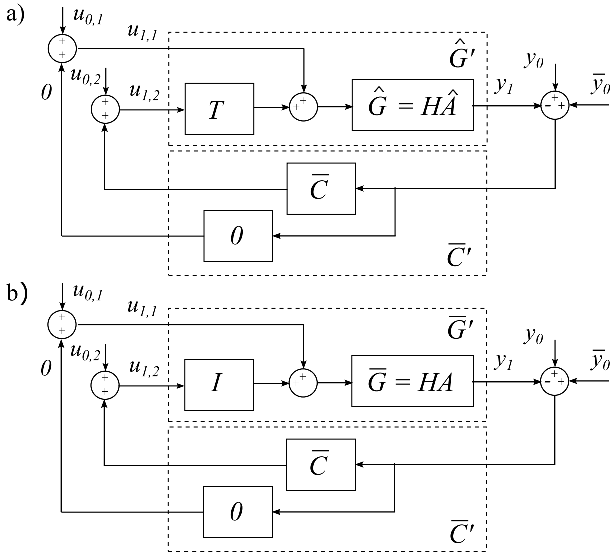

Fig. 17. Augmented ILC configurations corresponding to Fig. 16.

$$\Pi_{\bar{G}'//\bar{C}'} := \begin{pmatrix} u_{0,1}\\ u_{0,2}\\ y_0+\bar{y}_0\end{pmatrix} \mapsto \begin{pmatrix} u_{1,1}\\ u_{1,2}\\ y_1\end{pmatrix} \tag{59}$$

whose norm can be shown to be bounded as

$$\|\Pi_{\bar{G}'//\bar{C}'}\| = \left\|\begin{pmatrix} I\\ \bar{G}\end{pmatrix}(1+\bar{C}\bar{G})^{-1}(I,\bar{C})\right\| = \|\Pi_{\bar{G}//\bar{C}}\|.$$

Next, the gap between $\bar{G}'$ and $\hat{G}'$ is defined by

$$\delta(\hat{G}',\bar{G}') = \inf_{\Phi\in\Omega}\ \sup_{\substack{x\neq 0\\ x\in \mathrm{dom}(\hat{\mathcal{G}}')}} \frac{\|(\Upsilon-I)x\|}{\|x\|}$$

$$\le \inf_{\substack{\Phi\in\Omega\\ u_{1,1}=0}}\ \sup_{\substack{x\neq 0\\ x\in \mathrm{dom}(\hat{\mathcal{G}}')}} \frac{\|(\Upsilon-I)x\|}{\|x\|} = \delta(\hat{G}T(z,\theta),\bar{G})$$

where $\bar{\mathcal{G}}' := \left\{\begin{pmatrix} u_1\\ y_1\end{pmatrix} : y_1 = \bar{G}'u_1, u_1 \in \mathcal{U}\right\}$, $\hat{\mathcal{G}}' := \left\{\begin{pmatrix} u_1\\ y_1\end{pmatrix} : y_1 = \hat{G}'u_1, u_1 \in \mathcal{U}\right\}$, and $\Omega := \{\Upsilon : \hat{\mathcal{G}}' \mapsto \bar{\mathcal{G}}'\}$. This yields the stability condition

$$\delta(\hat{G}T(z,\theta),\bar{G}) \le \|\Pi_{\bar{G}//\bar{C}}\|^{-1} \tag{60}$$

which guarantees stability of Fig. 17a), and hence also Fig. 16a), since it implies $\delta(\hat{G}', \bar{G}') \leq \|\Pi_{\bar{G}'//\bar{C}'}\|^{-1}$. The property that T minimises the tracking error bounds can be seen by substituting $\delta(\hat{G}T(z,\theta), \bar{G})$ for $\delta(\hat{G}, \bar{G})$ in (56), and then inserting into (20) to obtain

$$\|\Pi_{\hat{G}//\bar{C}}\|_{\bar{w}_0} \leq$$

$$\|\Pi_{\bar{G}//\bar{C}}\|_{\bar{w}_0} \frac{1 + \delta(\bar{G^*}, \bar{G}) + \delta(\hat{G}T(z,\theta), \bar{G^*})}{1 - \|\Pi_{\bar{G}//\bar{C}}\|_{\bar{w}_0}(\delta(\bar{G^*}, \bar{G}) + \delta(\hat{G}T(z,\theta), \bar{G^*}))}$$

which is then minimised by (30). If $\text{range}(A) \subseteq \text{range}(\hat{A}(z,\theta))$, then $\hat{A}(z,\theta)\hat{A}^{\dagger}(z,\theta)A = A$ and so $\delta(\hat{G}T(z,\theta), \bar{G^*}) = 0$, and the original condition (18) and robustness bound (20) of Theorem 3 are retained.

ACKNOWLEDGMENT

The authors would like to thank Dr Junlin Zhou for his help implementing and conducting the experimental tests.

REFERENCES

[1] V. L. Feigin, M. Brainin, B. Norrving, S. Martins, R. L. Sacco, W. Hacke, M. Fisher, J. Pandian, and P. Lindsay, "World stroke organization (wso): Global stroke fact sheet 2022," *International journal of stroke*, 2022.

[2] E. S. Lawrence, C. Coshall, R. Dundas, J. Stewart, A. G. Rudd, R. Howard, and C. D. Wolfe, "Estimates of the prevalence of acute stroke impairments and disability in a multiethnic population," *Stroke*, vol. 32, no. 6, pp. 1279–1284, 2001.

[3] G. Kwakkel, B. J. Kollen, J. van der Grond, and A. J. H. Prevo, "Probability of regaining dexterity in the flaccid upper limb: impact of severity of paresis and time since onset in acute stroke." *Stroke*, vol. 34 9, pp. 2181–6, 2003.

[4] P. R. Wilkinson, C. D. Wolfe, F. G. Warburton, A. G. Rudd, R. S. Howard, R. W. Ross-Russell, and R. R. Beech, "A long-term follow-up of stroke patients," *Stroke*, vol. 28, no. 3, pp. 507–512, 1997.

[5] D. O. Hebb, *Organization of Behavior*. Psychology Press, 1949.

[6] R. Stockley, R. Peel, K. Jarvis, and L. Connell, "Current therapy for the upper limb after stroke: a cross-sectional survey of uk therapists," *BMJ Open*, vol. 9, no. 9, 2019.

[7] S. S. N. A. Programme, "Stroke care in England, Wales and Northern Ireland," King's College London Sentinel Stroke National Audit Programme, Tech. Rep., 2023.

[8] A.-M. Hughes, J. H. Burridge, S. Demain, C. Ellis-Hill, C. Meagher, L. Tedesco Triccas, R. Turk, and I. Swain, "Translation of evidence-based assistive technologies into stroke rehabilitation: Users' perceptions of the barriers and opportunities," *BMC health services research*, vol. 14, p. 124, 03 2014.

[9] J. Eraifej, W. Clark, B. France, S. Desando, and D. Moore, "Effectiveness of upper limb functional electrical stimulation after stroke for the improvement of activities of daily living and motor function: a systematic review and meta-analysis," *Systematic Reviews*, vol. 6, no. 40, 2017.

[10] O. A. Howlett, N. A. Lannin, L. Ada, and C. McKinstry, "Functional electrical stimulation improves activity after stroke: a systematic review with meta-analysis," *Archives of physical medicine and rehabilitation*, vol. 96, no. 5, pp. 934–943, 2015.

[11] J. McCabe, M. Monkiewicz, J. Holcomb, S. Pundik, and J. J. Daly, "Comparison of robotics, functional electrical stimulation, and motor learning methods for treatment of persistent upper extremity dysfunction after stroke: A randomized controlled trial," *Archives of Physical Medicine and Rehabilitation*, vol. 96, no. 6, pp. 981–990, 2015.

[12] B. W. Heller, A. J. Clarke, T. R. Good, T. J. Healey, S. Nair, E. J. Pratt, M. L. Reeves, J. M. van der Meulen, and A. T. Barker, "Automated setup of functional electrical stimulation for drop foot using a novel 64 channel prototype stimulator and electrode array: results from a gait-lab based study," *Medical engineering & physics*, vol. 35, no. 1, pp. 74–81, 2013.

[13] J. Malešević, M. Štrbac, M. Isaković, V. Kojić, L. Konstantinović, A. Vidaković, S. Dedijer Dujović, M. Kostić, and T. Keller, "Temporal and spatial variability of surface motor activation zones in hemiplegic patients during functional electrical stimulation therapy sessions," *Artificial organs*, vol. 41, no. 11, pp. E166–E177, 2017.

[14] M. Valtin, K. Kociemba, C. Behling, B. Kuberski, S. Becker, and T. Schauer, "RehaMovePro: A versatile mobile stimulation system for transcutaneous FES applications," *European Journal of Translational Myology*, vol. 26, no. 3, 2016.

[15] T. Ward, N. Grabham, C. Freeman, Y. Wei, A.-M. Hughes, C. Power, J. Tudor, and K. Yang, "Multichannel biphasic muscle stimulation system for post stroke rehabilitation," *Electronics*, vol. 9, no. 7, 2020.

[16] D. A. Hebert, J. M. Bowen, C. Ho, I. Antunes, D. J. O'Reilly, and M. Bayley, "Examining a new functional electrical stimulation therapy with people with severe upper extremity hemiparesis and chronic stroke: A feasibility study," *British Journal of Occupational Therapy*, vol. 80, no. 11, pp. 651–659, 2017.

[17] O. Schill, R. Rupp, C. Pylatiuk, S. Schulz, and M. Reischl, "Automatic adaptation of a self-adhesive multi-electrode array for active wrist joint stabilization in tetraplegic SCI individuals," in *2009 IEEE Toronto International Conference Science and Technology for Humanity (TIC-STH)*, 2009, pp. 708–713.

[18] C. Salchow, M. Valtin, T. Seel, and T. Schauer, "A new semi-automatic approach to find suitable virtual electrodes in arrays using an interpolation strategy," *European Journal of Translational Myology*, vol. 26, no. 2, Jun. 2016.

[19] S. O'Dwyer, D. O'Keeffe, S. Coote, and G. Lyons, "An electrode configuration technique using an electrode matrix arrangement for FES-based upper arm rehabilitation systems," *Medical Engineering & Physics*, vol. 28, no. 2, pp. 166–176, 2006.

[20] E. Imatz Ojanguren, E. Irigoyen, D. Valencia-Blanco, and T. Keller, "Neuro-fuzzy models for hand movements induced by functional electrical stimulation in able-bodied and hemiplegic subjects," *Medical Engineering & Physics*, vol. 38, 06 2016.

[21] C. T. Freeman, "Electrode array-based electrical stimulation using ILC with restricted input subspace," *Control Engineering Practice*, vol. 23, p. 32–43, 2014.

[22] X. Sun and C. T. Freeman, "Parameterised function ILC with application to stroke rehabilitation," *Control Engineering Practice*, vol. 145, p. 105878, 2024.

[23] C. T. Freeman, *Control System Design for Electrical Stimulation in Upper Limb Rehabilitation*. Springer International Publishing Switzerland, 2016.

[24] T. Feix, J. Romero, H.-B. Schmiedmayer, A. M. Dollar, and D. Kragic, "The GRASP taxonomy of human grasp types," *IEEE Transactions on Human-Machine Systems*, vol. 46, no. 1, pp. 66–77, 2016.

[25] C. T. Freeman and M. French, "Estimation based multiple model iterative learning control," in *2015 54th IEEE Conference on Decision and Control (CDC)*, 2015, pp. 6070–6075.

[26] J. Zhou, C. T. Freeman, and W. Holderbaum, "Multiple-model iterative learning control with application to stroke rehabilitation," *Control Engineering Practice*, vol. 154, p. 106134, 2025.

[27] L. Hodgins, C. T. Freeman, and Z. Belkhatir, "Multiple model iterative learning control of FES electrode arrays," *21st international conference on informatics in control, automation and robotics*, 2024.

[28] F. Le, I. Markovsky, C. T. Freeman, and E. Rogers, "Identification of electrically stimulated muscle models of stroke patients," *Control Engineering Practice*, vol. 18, no. 4, pp. 396–407, 2010.

[29] C. T. Freeman, A.-M. Hughes, J. Burridge, P. Chappell, P. Lewin, and E. Rogers, "A model of the upper extremity using FES for stroke rehabilitation," *Journal of biomechanical engineering*, vol. 131, p. 031011, 04 2009.

[30] K. An, Y. Ueba, E. Chao, W. Cooney, and R. Linscheid, "Tendon excursion and moment arm of index finger muscles," *Journal of Biomechanics*, vol. 16, no. 6, pp. 419–425, 1983. [Online]. Available: https://www.sciencedirect.com/science/article/pii/002192908390074X

[31] D. A. Bristow, M. Tharayil, and A. G. Alleyne, "A survey of iterative learning control," *IEEE Control Systems Magazine*, vol. 26, no. 3, pp. 96–114, 2006.

[32] Y. Chen, B. Chu, C. T. Freeman, and Y. Liu, "Generalized iterative learning control with mixed system constraints: A gantry robot based verification," *Control Engineering Practice*, vol. 95, 02 2020.

[33] C. T. Freeman, "Robust ILC design with application to stroke rehabilitation," *Automatica*, vol. 81, pp. 270–278, 2017.

[34] J. L. M. Neto and T. Boaventura, "A brief survey of the gap metric for stability analysis," in *Simpósio do Programa de Pós-Graduação em Engenharia Mecânica - SIPGEM*. EESC-USP, 2019.

[35] T. T. Georgiou and M. C. Smith, "Robustness analysis of nonlinear feedback systems: An input–output approach," *IEEE Transactions on Automatic Control*, vol. 42, no. 9, p. 1200–1221, 1997.

[36] M. Kutlu, C. T. Freeman, E. Hallewell, A.-M. Hughes, and D. S. Laila, "Upper-limb stroke rehabilitation using electrode-array based functional

electrical stimulation with sensing and control innovations," *Medical Engineering & Physics*, vol. 38, no. 4, pp. 366–379, 2016.

[37] K. L. Meadmore, T. A. Exell, E. Hallewell, A.-M. Hughes, C. T. Freeman, M. Kutlu, V. Benson, E. Rogers, and J. H. Burridge, "The application of precisely controlled functional electrical stimulation to the shoulder, elbow and wrist for upper limb stroke rehabilitation: a feasibility study," *J Neuroeng Rehabilitation*, vol. 11, no. 105, pp. 1–11, 2014.

[38] D. Buchstaller and M. French, "Robust stability for multiple model adaptive control: Part i—the framework," *IEEE Transactions on Automatic Control*, vol. 61, no. 3, pp. 677–692, 2016.

[39] J. C. Willems, "Deterministic least squares filtering," *Journal of Econometrics*, no. 118, pp. 341–370, 2004.

[40] E. D. Sontag, *Mathematical Control Theory*. Springer, 1998.

[41] A. Soska, "Surface electrode array-based electrical stimulation and iterative learning control for hand rehabilitation," Ph.D. dissertation, University of Southampton, 2014.

[42] E. Theodorou, E. Todorov, and F. J. Valero-Cuevas, "Neuromuscular stochastic optimal control of a tendon driven index finger model," in *Proceedings of the 2011 American Control Conference*. IEEE, 2011, p. 348–355.

[43] J. Zhou, "Multiple model control of functional electrical stimulation electrode arrays," Ph.D. dissertation, School of Electronics and Computer Science, University of Southampton, 2025.

[44] D. Murdock, *Worked Examples from Introductory Physics Vol. IV: Electric Fields*. Tenn. Tech. Univ., 2008.

E BIOGRAPHY SECTION

Lucy Hodgins received an MEng degree in biomedical electronic engineering from the University of Southampton in 2023. She is currently studying towards a PhD in electrical and electronic engineering at University of Southampton. She is a member of IEEE as well as the Institute of Engineering and Technology (IET), and is part of the IEEE Control Systems Society NextCom committee. Her research interests cover the identification and control of biomedical systems, and she acts as host of the academic podcast Coffee and Control.

Chris Freeman received the BEng. degree in Electromechanical Engineering in 2000, the PhD degree in Applied Control in 2004, both from the University of Southampton, and the BSc degree in Mathematics from the Open University in 2006. He is currently Professor of Robotics and Control at the University of Southampton, United Kingdom. His research interests include the development, application and assessment of iterative learning and repetitive controllers within both the biomedical engineering domain and for application to industrial systems. He has 310 refereed conference and journal papers in these areas.

Zehor Belkhatir received her Engineering and MSc degrees in Automatic Control from Ecole Nationale Polytechnique, Algiers, Algeria, in 2012, and her PhD degree in Electrical Engineering from King Abdullah University of Science and Technology, Jeddah, Saudi Arabia, in 2018. From 2018 to 2020, she held a Postdoctoral Research Scholar Position with the Department of Medical Physics at Memorial Sloan Kettering Cancer Center, New York, United States. She is currently a lecturer (Assistant Professor) with the School of Electronics and Computer Science, University of Southampton, United Kingdom. Her research interests span the fields of applied mathematics, control systems theory, and data analysis. She is particularly interested in developing control, estimation and computational data analytics techniques for robotic and biomedical systems. She is a member of the Technology Conferences Editorial Board (TCEB) and the European Control Association (EUCA) Conference Editorial Board.